Radar Survey of Hail-Producing Storms and Environments during the 2018–19 Severe-Weather Season in the Córdoba Region of Argentina

Calvin M. Elkins[a,b] and Deanna A. Hence[a]

[a] University of Illinois, Urbana–Champaign, Urbana, Illinois
[b] 557th Weather Wing, Offutt Air Force Base, Nebraska

(Manuscript received 15 August 2023, in final form 2 January 2024, accepted 19 February 2024)

ABSTRACT: Frequent deep convective thunderstorms and mesoscale convective systems make the Córdoba region, near the Sierras de Córdoba mountain range, one of the most active areas on Earth for hail activity. Analysis of hail observations from trained observers and social media reports cross-referenced with operational radar observations identified the convective characteristics of hail-producing convective systems in central Argentina over a 6-month period divided into early (October–December 2018) and late seasons (January–March 2019). Reflectivity and dual-polarization characteristics from the Córdoba operational radar [Radar Meteorológico Argentina (RMA1)] were used to identify the convective modes of convective cells at time of positive hail indicators. Analysis of ERA5 upper-air and surface data examined convective environments of hail events and identified representative dynamic and thermodynamic environments. A majority of early season hail-producing cells were classified as discrete convection, while discrete and multicell occurrence evened out in the late season. Most hail-producing cells initiated directly adjacent to the Sierras in the late season, while cell initiation and hail production is further spread out in the early season. Dividing convective events into dynamic/thermodynamic regimes based on values of 1000 J kg^{-1} of CAPE and vertical wind shear of 20 m s^{-1} results in most early season events reflecting shear-dominant characteristics (low CAPE, high shear) and most late-season events exhibiting CAPE-dominant characteristics (high CAPE, low shear). Strength and placement of low-level temperature and moisture anomalies/advection and upper-level jets largely defined the differences in the dominant regimes.

SIGNIFICANCE STATEMENT: This study used regional radar data alongside hail reports from trained observers and social media to better understand the types and timing of storms identified as producing hail, given the lower resolution of satellite studies. Dividing the hail season (October–December; January–March) showed that within hail season, early season storms tended to be singular storms that formed across the region in environments with strong vertical winds and weak instability. Late-season storms were a mix of singular storms and multicellular storm systems focused on the mountains in weak vertical winds and strong instability. These results show differences from satellite studies and identify key representative hail-producing radar features and environmental regimes for this region, which could guide hail risk analysis within the severe-weather season.

KEYWORDS: South America; Synoptic-scale processes; Convective storms; Hail; Radars/Radar observations; Operational forecasting

1. Introduction

Severe convective weather near the Córdoba region of central Argentina is unique owing to the frequent development, strength, and size of local thunderstorms and mesoscale convective systems (Velasco and Fritsch 1987; Zipser et al. 2006). Global satellite hail studies and climatologies (Cecil 2009; Cecil and Blankenship 2012; Bruick et al. 2019) identified the area stretching from Mendoza to Córdoba as possibly the most active hail-producing region on Earth. Ground observation-based hail climatological studies in and around Argentina (Mezher et al. 2012; Martins et al. 2017) confirmed that this region sees frequent hailstorms, often featuring hailstones ≥ 7.5 cm or 3 in. [Kumjian et al. 2020; M. Runga, Servicio Meteorológico Nacional de Argentina (SMN), 2018, personal communication]. However, while these climatologies examined synoptic conditions associated with diurnal or seasonal variations, few studies focused on storm convective modes or environmental parameters responsible for hail in this region.

Analysis of convective modes with ground-based radar became possible in the Córdoba region with the installation of the first Radar Meteorológico Argentino (RMA1) C-band radar within the city of Córdoba in 2015 (P. Salio 2018, personal communication). The 2018–19 Remote Sensing of Electrification, Lightning, And Mesoscale/Microscale Processes with Adaptive Ground Observations–Cloud, Aerosol, and Complex Terrain Interactions (RELÁMPAGO-CACTI; hereafter RELÁMPAGO) field campaign (Nesbitt et al. 2021; Varble et al. 2021) collected observations of convective initiation, upscale growth, high-impact weather, and hydrology related

---

Denotes content that is immediately available upon publication as open access.

Supplemental information related to this paper is available at the Journals Online website: https://doi.org/10.1175/JAMC-D-23-0140.s1.

Corresponding author: Calvin M. Elkins, calvin.elkins.wx@gmail.com

DOI: 10.1175/JAMC-D-23-0140.1

to the region's deep convection. With data collected from RELÁMPAGO, Mulholland et al. (2018, hereafter M18) presented a ground-based radar-focused study on storm modes and structure in the Córdoba region, though not specifically focused on hail. Using a combination of RELÁMPAGO observations and hail reports gleaned from social media, this study builds on the convective mode analysis in M18 to determine the storm structures and environments most responsible for central Argentina's hail production during the 2018–19 hail season.

As a survey of 6 months of radar observations and reanalysis data, this study quantifies the frequency and spatial distribution of convective modes most responsible for hail production during this timeframe alongside the concurrent storm parameters and composite synoptic environments. This combination allows an assessment of the accompanying seasonal environments that gives insight into the modes and storm parameters [e.g., vertical wind shear (VWS) and convective available potential energy (CAPE)] that generated hail in the Córdoba region during this study. Section 2 details the radar and storm report dataset and expands on the methodology of database construction and analysis. Section 3 examines the results of classification, and section 4 details environmental analysis and discusses implications for forecasting use. Summary and conclusions are in section 5.

2. Storm report database, convective mode identification, and convective event classification

a. *Storm report databases*

For this survey, we constructed a database of potential hail-producing storm cells within the range of RMA1 between October 2018 and March 2019. This timeframe was chosen because of its overlap with RELÁMPAGO (October–December 2018), which provided high-density and reliable storm observations from trained meteorologists. To allow the storm report dataset to encapsulate the entire October–March hail season, we supplemented the RELÁMPAGO observations with a combination of Twitter data and operational radar data (see section 2b). For the Twitter data, we used internet search optimization software Brandwatch (formerly Crimson Hexagon) to create detailed searches of hail-related Twitter posts (search parameters available in the online supplemental material). Twitter was chosen because of its status at the time as the social media platform best set up for real-time dissemination of quickly changing news and information (Fraustino et al. 2012; Liu et al. 2016; Pavlov et al. 2018). Complications resulting from the COVID-19 pandemic (see conclusions in section 5) limited this analysis to the 2018–19 severe-weather season.

When searching with Brandwatch, the search parameters included the word "hail," Spanish words commonly related to hail (e.g., granizo and piedra), and names of communities within the RMA1 radar range (e.g., Córdoba and Villa Carlos Paz). After retweets were eliminated, we manually examined each individual tweet for information that could be interpreted as real-time reports of hail and where timing and location of the potential cell could be corroborated by radar. Once identified, the tweet was documented for future analysis of the region's weather community social media activity.

b. *Córdoba RMA1 radar, potential hail event identification, and cell tracking*

RMA1 is a C-band (5.4-cm wavelength), dual-polarization Doppler radar located in the city of Córdoba, Córdoba, Argentina, and operated by Sistema Nacional de Radares Meteorológicos (SINARAME) for SMN (location marked by star in Fig. 1). RMA1 is a simultaneous transmit and receive radar, with a beamwidth of 0.98° and 480-m spacing between gates. RMA1 employs three scan strategies: a three-angle high-resolution scan in the "Optimo" range (~93 km), a full volume scan in the "Doppler" range (~223 km), and a maximum range scan (~480 km; P. Salio, personal communication). During this research, data were limited to the Optimo and Doppler scans to minimize the impacts of beam height and spreading. RMA1 data were quality controlled using the National Center for Atmospheric Research (NCAR) SOLO software to ensure that all echoes analyzed were meteorological events; radar artifacts and echoes deemed ambiguous were discarded.

Because hail identification in this study depends largely on radar detection, it is important to note that hail identification, hail indicators, and any analysis that speaks to the possibility of a cell-containing hail is not to be taken as an indication of actual hailfall at the ground. The use of potential hail indicators beyond direct confirmation from the RELÁMPAGO observers was important due to the temporal and logistical limitations of the campaign (researchers were limited to 3 months of work with their equipment; it is not possible to intercept each storm of interest). The two radar-centric methods of potential hail-containing cell identification [see sections 2b(1) and 2b(2)] used a combination of favorable dual-polarized parameters and the identification of a three-body scatter spike (3BSS; Zrnić 1987; Wilson and Reum 1986, 1988; Lemon 1998). To maximize the likelihood of a radar-identified cell being a hail producer, several factors (attenuation, beam range, and beam height with respect to melting level) had to be accounted for.

C-band radars are subject to attenuation, differential attenuation, non-Rayleigh scattering, and backscatter differential phase effects (Fabry 2015; Rauber and Nesbitt 2018). Therefore, cells identified as possible hail containers were subject to careful analysis before being placed into the database. Since beam attenuation results in false values (Ryzhkov et al. 2013), a simple linear radar correction based on differential phase values (K_{DP}; Carey et al. 2000; Gematronik 2007) was applied to target cells to measure the effects of attenuation on reflectivity Z_h and differential reflectivity Z_{DR}. Any effects of attenuation would lead to an underrepresentation of possible hail-containing cells as Z_h and Z_{DR} values along an attenuated beam would be lower. Most cells in this study (~79%) suffered little effect from attenuation. The ~21% of cells that did appear along more highly attenuated radar beams saw value shifts (2.5–4.0 dBZ for Z_h and 0.5–1.0 dB for Z_{DR}). For this work, the attenuation effect on Z_h had no effect on cell identification and tracking. Additionally, the Z_{DR} correction did not move cells out of the potential database, but it did move some cells to different cell identification criteria [see section 2b(1)].

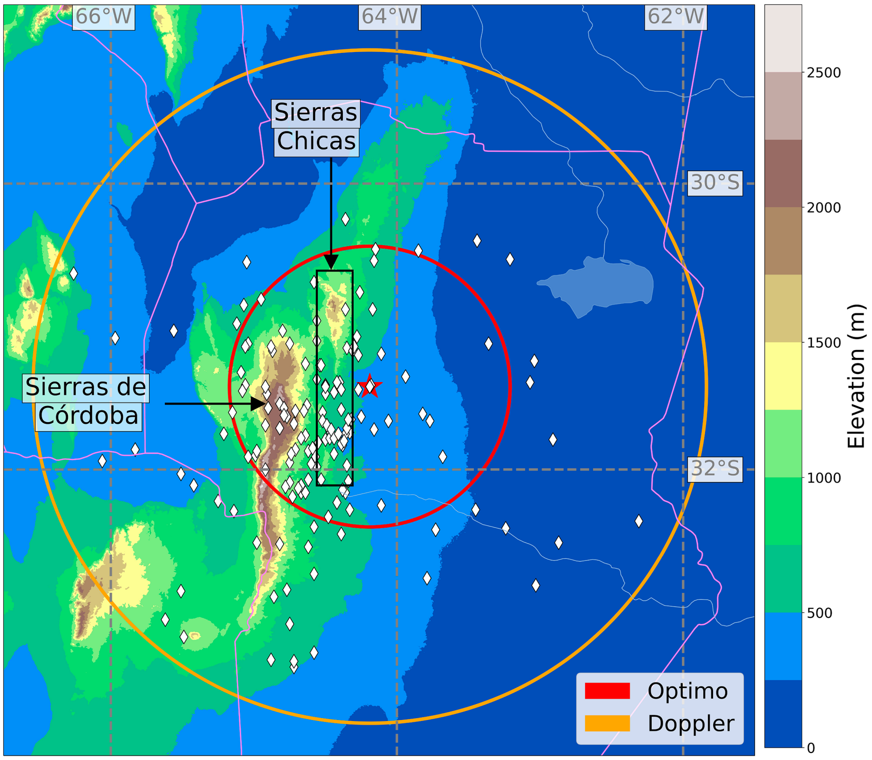

FIG. 1. Map of the domain for the RMA1 radar (red star), with provincial borders (pink) and waterways (gray). The locations of both the SdC and the Sierras Chicas are indicated. The red and orange circles outline the range of RMA1's Optimo and Doppler scan ranges, respectively. White diamonds represent the locations where the presence of hail was suggested through a trained observer, Twitter, or radar observations.

Additionally, measuring the distance between potential cells and RMA1 allowed the calculation of the height of the possible hail signature. Combining measured height with the altitude of the melting layer [see section 2d(1)] allowed the classification of each cell by its relationship to the melting layer. Analysis of Z_{DR} values against range and height with respect to the melting layer (available as supplemental data) showed that most cells with Z_{DR} values between -1 and 1 dB were near or above the melting layer, and that as Z_{DR} increased, cell height (with respect to the melting layer) decreased. Accordingly, the further from RMA1 a cell was, the more likely it was to have low Z_{DR} values, indicating the radar beam intersecting storms above the melting level. Overall, for cells further away from RMA1, the radar beam was unable to scan at lower levels, limiting the available dual-polarized indicators, leading to potential hail-producing cells not being identified.

1) DUAL-POLARIZED PARAMETER CELL IDENTIFICATION

According to Rauber and Nesbitt (2018), the most favorable combinations of dual-polarized parameters to detect hail require a high radar reflectivity ($Z_h \geq 50$ dBZ) collocated with key values of differential reflectivity ($Z_{DR} \sim 0$ dB for dry hail, as high as 3–8 dB in the presence of large hail or wet hail for C-band radars; Anderson et al. 2011), along with correlation coefficient ($\rho_{HV} \sim 0.9$; can be lower for large hail and higher for small hail) and specific differential phase ($K_{DP} \sim 1$; can be higher for melting hail). The difference in Z_{DR} at different heights (with respect to the melting level) is important as it gives two "bins" for classification: potential hail above the melting level and potential hail below the melting level.

Ultimately, we created two schemes to identify a potential hail-containing cell based on dual-polarized data. For Z_{DR} between -1 and 1 dB (likely above or near the melting level), $Z_h \geq 50$ dBZ, ρ_{HV} was 0.85–0.95, and K_{DP} was 0–2. For Z_{DR} above 1 dB (likely near or below the melting level), $Z_h \geq 50$ dBZ, ρ_{HV} was 0.80–0.95, and K_{DP} was 0–4.

2) THREE-BODY SCATTER SPIKE CELL IDENTIFICATION

As RMA1 is a C-band radar, it is possible for both large raindrops and hailstones to cause the three-way scattering of the radar beam (Lemon 1998). When comparing C band to S band, Kaltenboeck and Ryzhkov (2012) showed that C band had a more pronounced 3BSS due to the contribution of resonant scatterers, but still identified the spike as an attribute of hail. Additionally, only half of the cells identified through

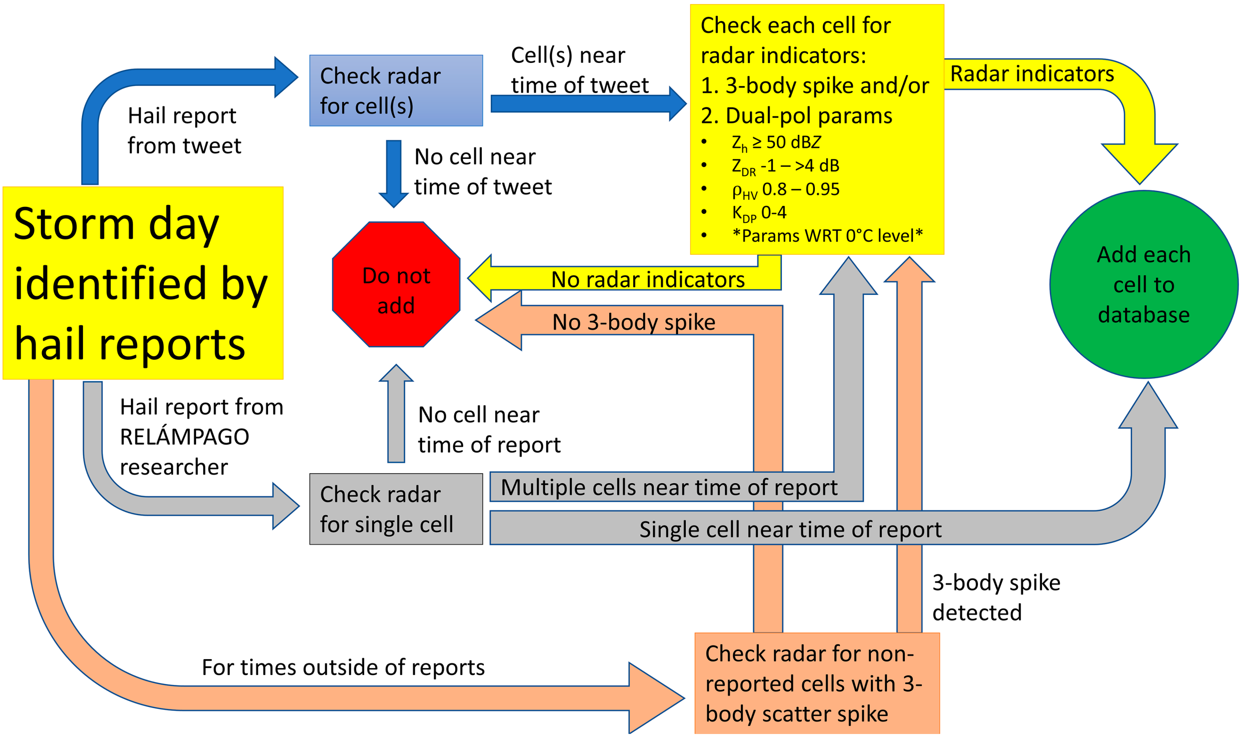

FIG. 2. Flow diagram of methodology used to construct the hail databases. Storm days were identified by tweets that could be investigated for hailfall or a report from a RELÁMPAGO researcher. For every day with a positive report, times outside of those reports were examined for indicators of a 3BSS.

observations by RELÁMPAGO researchers featured a 3BSS, which shows that relying solely on this method could cause both over- and underestimation of hail-producing systems. To mitigate these biases, we limited the use of 3BSS to days in which there was a hail report through RELÁMPAGO observations or through Twitter. This limitation heightened the likelihood that the environment being investigated with the hail spike was one in which hail-containing cells existed. Identified cells were then examined with the same dual-polarized parameter scheme detailed in the previous section.

3) DATABASE CREATION AND CELL TRACKING

Based on the three hail recognition methods—RELÁMPAGO observations, Twitter data combined with radar data, and radar data alone—we determined their levels of reliability. The method assumed most trustworthy, yet most spatially and temporally limited, was direct hail observations by RELÁMPAGO researchers. The next method was using Twitter data in conjunction with radar data (dual-polarized identification) to examine the time and area of the tweet. Finally, the least reliable method was to rely solely on the 3BSS identification path. Each cell identified was indexed with the marker of the highest reliability method that was used to identify it.

Individual cells were determined as potential hail containers through the process detailed in Fig. 2. A “storm day” was defined as a day with either confirmed hail (RELÁMPAGO report) or hail identified by a Twitter report with a corresponding favorable radar signature. For observations or tweets, we examined RMA1 data around the time of the report to determine if a cell moved near the identified area. If so, and the cell corresponded with a report from a trained observer, the storm was added to the database. If so and the cell corresponded with a tweet, the cell was further examined for radar indicators [sections 2b(1) and 2b(2)]. If the identification was positive, the storm was added to the database; if multiple cells moved over the area, each individual cell had to also display a positive indicator to be added. The day—as defined by 0000–2359 UTC (cells and systems that were a clear continuation of events prior to 0000 UTC were counted as the previous day)—was then further examined for any other cells that displayed a 3BSS, which were then investigated for inclusion.

Once a cell was identified as a potential hail container, the storm was assigned a convective mode based on whether it was a discrete cell at the time of detected hail or part of a multicell system (see section 2c). The cell was then manually tracked to its origin point, defined as the first 35-dB*Z* echo (appendix A). The time and location of origin and the initiation mode were then recorded. Note that the hail report time is not necessarily the first time that the cell produced hail; it is the time at which the possible presence of hail was indicated by one of the preceding methods. Further, if a cell entered RMA1’s range already initiated, full tracking could not be done.

c. Storm convective mode classification

Past studies used radar reflectivity signatures to identify and classify storm modes (Bluestein and Jain 1985; Trapp et al. 2005; Gallus et al. 2008; Smith et al. 2012; M18). For this study, storm mode classification was applied at the time of the earliest indicator of hail. While M18 served as a starting point for this research, their study subdivided discrete and multicells into smaller categories based on rotation and organization/contiguity and used a distance of 25 km for separating convective cores. Owing to the 4 m s^{-1} Nyquist velocity of the Doppler scan pattern of RMA1 making it difficult to determine rotation and potential mesocyclones for more distant storms, radial velocity was not considered for storm analysis in this study, resulting in fewer subdivisions for classification categories.

A discrete cell had to display reflectivity ≥ 35 dBZ and be isolated from other cells (no contiguous reflectivity). However, the cell would still be considered a discrete cell if it shared any area of contiguous reflectivity < 20 dBZ with another cell that displayed a ≥35-dBZ core at any scan level, if the adjacent ≥35-dBZ core was at least 30 km away. Ideally, the discrete cell would not share any contiguous areas of reflectivity, but cellular convection occasionally initiates near and merges with other convective cells.

Multicell systems had to display contiguous areas of reflectivity ≥ 35 dBZ over 15 km, be a group of cells that were less than 30 km from each other, and/or be cells that shared contiguous reflectivity ≥ 20 dBZ with another cell that displayed a core ≥ 35 dBZ within 30 km. These definitions cover multicell events such as mesoscale convective complexes.

d. Convective event identification

During the study, some days featured multiple hail-producing cells. To avoid biases in the storm environment composite analysis, individual cells were grouped into convective events. Cells were grouped based on similarities between radar-indicated initiation time and location as well as similarities in upper-air soundings, surface wind flow (including mountain interactions), and proximity to boundaries determined from reanalysis data (appendix B). For the purposes of calculating means and medians, storm parameter values taken near each cell [e.g., CAPE and VWS; section 2d(1)] were averaged with all others within the same convective event. This allowed each event (as opposed to each cell) to be used in calculating monthly and seasonal averages. For some cases, a single cell encapsulated an entire convective event.

Classification of convective events fell into three categories: exclusive, mixed-modes, and inclusive. A discrete or multiexclusive event (DE/ME) would count events housing only discrete or multicells, respectively. Mixed-mode events (XI) would count only those events that feature both discrete and multicell convection. Last, inclusive events (not shown, but used for calculations) would combine the exclusive mode of choice with mixed-mode events (e.g., DE + XI = discrete inclusive), thereby giving consideration to all events that contained the target convective mode. For the calculations of mean seasonal values, each convective event would be counted once (i.e., DE + ME + XI). For the calculation of environmental anomalies, inclusive events were used to ensure that all atmospheric makeups supporting the chosen type of convection were represented. Convective events will be expanded on in section 3b.

SURFACE, UPPER-AIR, AND TOPOGRAPHIC DATA

We used ERA5 (Hersbach et al. 2020) reanalysis data to assess the mesoscale and synoptic-scale environments (upper-air and surface) in the Córdoba region on investigated storm days. ERA5 is a global atmospheric reanalysis dataset created by and available through the European Centre for Medium-Range Weather Forecasts (ECMWF) that provides hourly and monthly averaged upper-air and surface data using 4D-Var data assimilation on 37 available pressure levels.

We created simulated soundings from reanalysis data using the MetPy software package (May et al. 2020) to align thermodynamic observations more precisely to the location and time of the convection. Operational and RELÁMPAGO soundings were limited by launch times and locations that frequently failed to align with the convection of interest and were thus not used for this study. ERA5 data were taken from the grid point closest to the storm, using the hour in which storm initiation was recorded. If the grid point was not representative of the storm environment due to large differences in elevation or spatial differences resulting from terrain (such as points being on different sides of mountains), the other nearest grid points were investigated for more representative settings. Additionally, if soundings contained unrealistic environmental parameters (such as 0 CAPE), data at that grid point were examined within a ±2-h window.

Reanalysis soundings were analyzed for similarities in the vertical distribution of temperature/humidity as well as to calculate common storm environmental parameters such as most unstable and surface-based CAPE, VWS values over different levels, and precipitable water (PWAT). VWS was calculated from the surface to the 500-hPa level as a proxy for 0–6-km shear (Evans and Doswell 2001) to address points above high elevation. If calculation of most unstable CAPE returned unrealistic values (e.g., 0 CAPE), then we used the surface-based CAPE calculated by ERA5. Py-ART (Helmus and Collis 2016) was then used to calculate anomalies in monthly and seasonal mean values. Topographic data were obtained from the U.S. Geological Survey (USGS) digital elevation models.

3. Convective modes for hail-containing cells and convective events

a. Counts and distributions of hail-containing cells

A total of 162 individual potential hail-containing cells were recorded over the study period (Fig. 3). For 23 cells, the primary hail recognition method was through observations by researchers during RELÁMPAGO. An additional 53 cells were identified by the combination of Twitter and radar data. The final 86 cells were primarily identified by the 3BSS path. Of the cells sampled, 63% (102 total) occurred in the early season (October–December) and 37% (60 total) in the late season (January–March). This seasonality was also present when examining discrete versus multicells. In the early

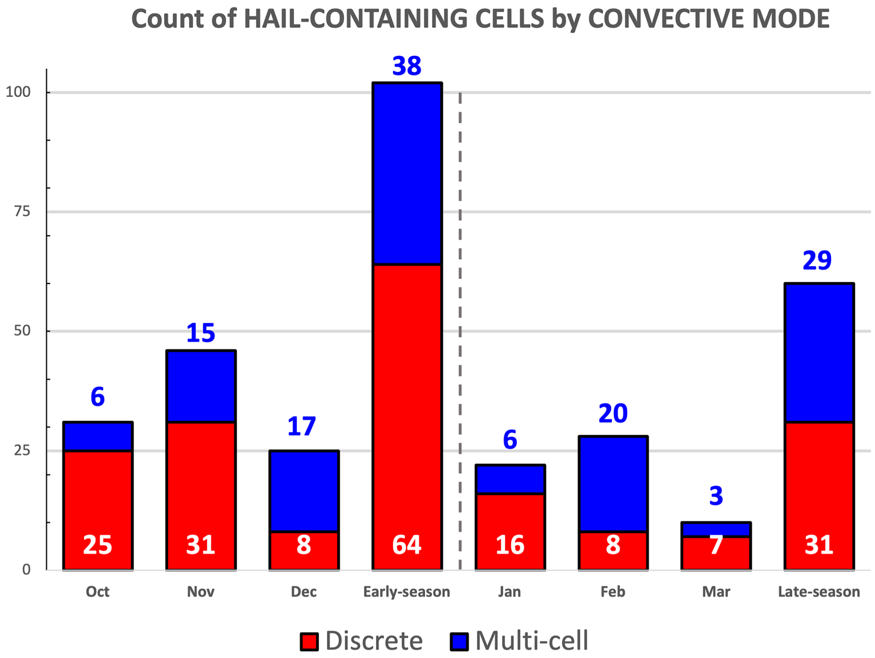

FIG. 3. Monthly and seasonal counts of hail-containing storm cells by convective mode.

season, discrete made up 63% of the recorded cells, but in the late season, the split was virtually even.

Of the 162 cells, 145 could be tracked from initiation to positive identification. Altogether, most of these 145 viable storm tracks passed near the vicinity of the Sierras de Córdoba (SdC) and the Sierras Chicas (Fig. 4). However, in the early season, storm paths were spread around the domain, including the valley to the west of the Sierras and the plains to the east. Late-season paths were mostly contained to areas closer to the SdC. This pattern was further reinforced by the fact that of the 102 early season cells, 16 were nontrackable (initiating outside of RMA1's range), while only 1 of the 60 late-season cells was nontrackable. It should be noted that longer tracks mean that the storm took longer to show a

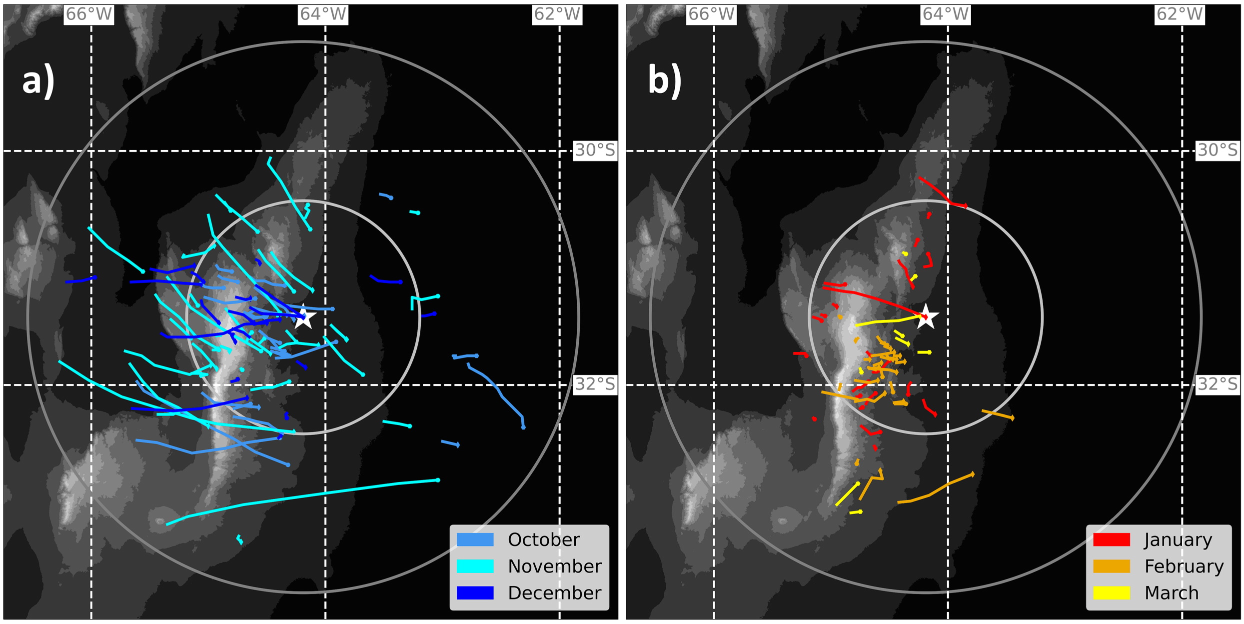

FIG. 4. Path of hail-producing cells as tracked from cell initiation to positive identification for the periods of (a) October–December and (b) January–March. Terrain elevation (gray), RMA1 location (star), and range rings (circles) are the same as in Fig. 1. Cells that could not be tracked to initiation are not included.

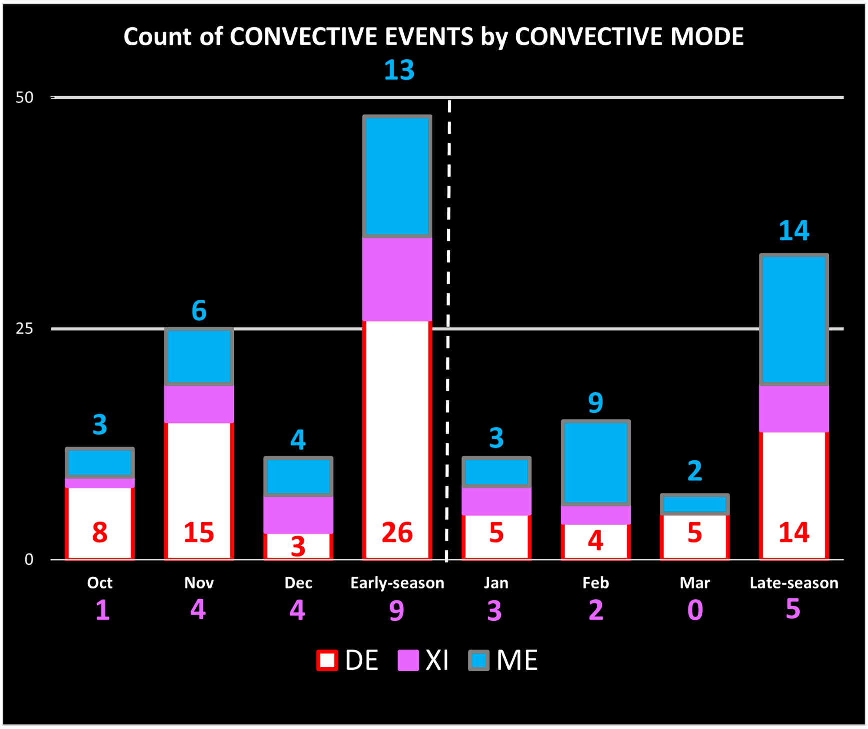

FIG. 5. Monthly and seasonal counts of convective events.

positive indicator, not that it necessarily took longer to produce hail.

b. Distribution of convective events

The grouping of multiple individual cells into convective events (section 2d) resulted in 81 total convective events, with 48 occurring in the early season and 33 in the late season (Fig. 5). The seasonal distribution of (inclusive) convective events is approximately proportional to that of individual cells, despite a few days in this study featuring a large number of cells (e.g., both 18 October 2018 and 22 February 2019 had over 10 cells recorded). That the proportionality of cells to events remained similar indicates that a few outlier case days did not introduce large biases.

DE outnumbered ME in the early season (26–13 with 9 XI), but the count was even in the late season (14–14 with 5 XI). Overall, 14 of the 81 events featured multiple convective modes, with no apparent seasonality (19% of early season cases and 15% of late-season cases). These findings show early season similarity with M18 which noted that discrete were favored in the early season. However, their findings noted more late-season multicells than discrete at an approximate 2:1 ratio, while the count was even in this study.

4. Analysis of mesoscale and synoptic-scale environments

a. Intraseasonal variations in convective event parameters

CAPE, VWS (specifically, 0–6 km), and PWAT are generally accepted as globally important parameters for hail production (Allen et al. 2011; Tuovinen et al. 2015; Li et al. 2018). Therefore, these were the three parameters chosen for consideration to further investigate the seasonal differences between convective events. Examination of mean CAPE and VWS values per convective mode showed a strong dichotomy between seasons (Figs. 6 and 7). In the early season (Fig. 6), there was little difference in the mean values of CAPE or VWS between the convective event classifications, indicating that these two parameters were not significant determiners of early season convective modes. While there was an overall drop in VWS values in the late season (Fig. 7), there still was not a large spread in values across categories. However, there was a greater spread in CAPE. CAPE for ME events (1066 J kg^{-1}) was very low compared to the late-season mean (1385 J kg^{-1}), while DE was very close to the mean value (1398 J kg^{-1}). XI's status as an outlier (2239 J kg^{-1}) could indicate that CAPE values much higher than the mean can simultaneously support both kinds of convection better than lower values.

In contrast to CAPE, PWAT showed a more subdued seasonal change. In general, PWAT values were higher for multicell classification as opposed to discrete. Values across the board increased from the early season to the late season for each category, ranging from a 1.1-mm difference (DE) to a 6.4-mm difference (XI). The large jump in XI PWAT combined with its large late-season CAPE value may indicate a marker for mixed convection in the late season.

These variations in storm parameters from convective events corresponded well with monthly shifts in both CAPE and VWS (Fig. 8). Median CAPE for each month in the early season was

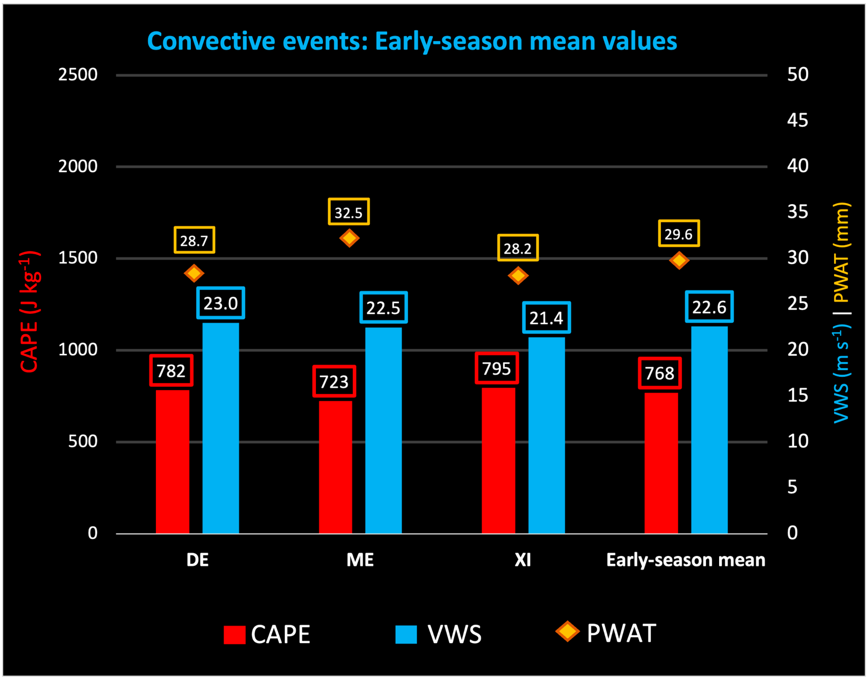

FIG. 6. Mean values of CAPE (J kg^{-1}), surface-to-500-hPa VWS (m s^{-1}), and PWAT (mm) for convective events in the early season.

less than 1000 J kg^{-1}, while for January and February, the medians were greater than 1000 J kg^{-1}. March showed a large spread of values (over only seven total events), but its median was still close to 1000 J kg^{-1}. November–January boasted wide ranges of CAPE values within the 25th–75th percentile range, as well as the highest outliers, presumably showing the volatility of the environment moving from one season to the next. For VWS, each month in the early season had median

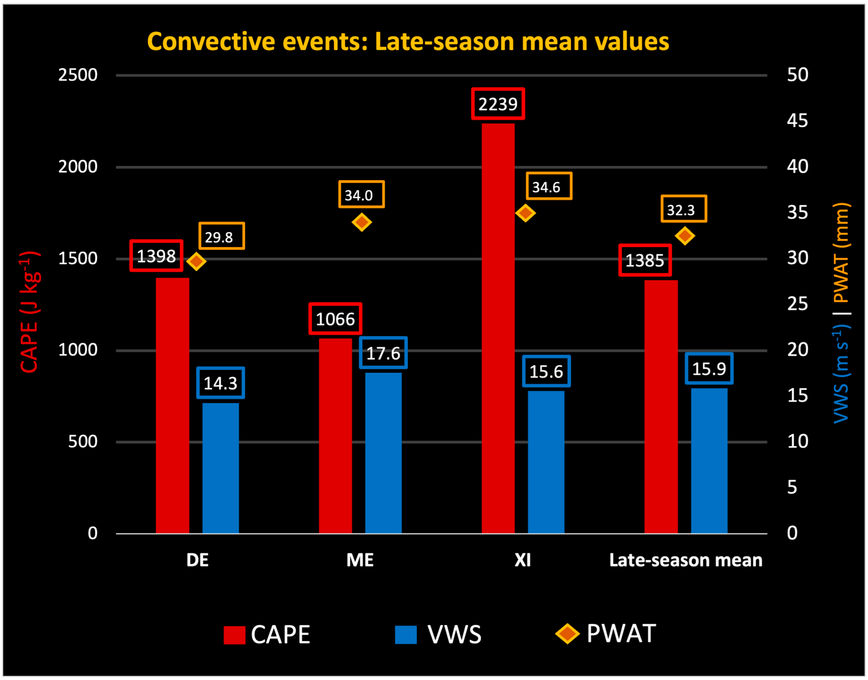

FIG. 7. Mean values of CAPE (J kg^{-1}), surface-to-500-hPa VWS (m s^{-1}), and PWAT (mm) for convective events in the late season.

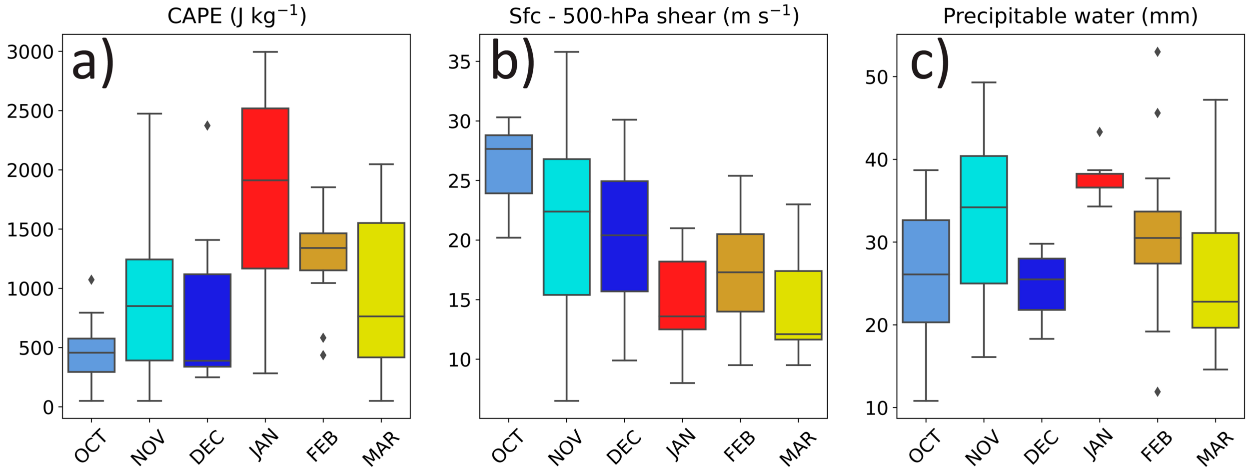

FIG. 8. Monthly distribution of (a) CAPE, (b) surface-to-500-hPa VWS, and (c) PWAT for convective events. The box bounds the 25th and 75th percentile, with the line indicating the median value. Whiskers include values within 1.5 interquartile range from the box, and diamonds indicate the values outside of this range. For (c), January median equals the value at the 25th percentile.

values greater than 20 m s^{-1}, and all months in the late season had medians less than 20 m s^{-1}. Despite January's median and spread being lower than February, there was still a clear, linear descent in VWS values from October through March.

PWAT showed seasonal signals similar to CAPE with a relative rise in values from October peaking in January. This suggests that the mechanisms responsible for the increase (decrease) in CAPE may also result in an increase (decrease) in PWAT. While the variations do not follow a smooth pattern (with December values generally lower than November), it should be reiterated that this is a study taken over one severe-weather season. Furthermore, the observed PWAT values of Schumacher et al. (2021) confirm the monthly calculated PWAT means seen in Fig. 8. The fact that the 25th percentile for all given months was ~20 mm or above suggests that this value could serve as a forecasting baseline for how much environmental PWAT is normally necessary for hail formation.

These results, when combined with the findings in Figs. 6 and 7, showed two distinct setups: the low-CAPE, high-shear environment of the early season and the high-CAPE, low-shear environment of the late season. These CAPE/shear setups, as mentioned above, indicate break points at 1000 J kg^{-1} and 20 m s^{-1}. These general setups are similar to severe-weather setups in the United States for bow echoes ("dynamic" bow echoes forming in the low-CAPE, high-shear "cool season" and "progressive" bow echoes forming in the high-CAPE, low-shear "warm season"; Johns 1993) and will be referred to as "shear dominant" (SDOM) and "CAPE dominant" (CDOM), respectively.

b. *Characteristic dynamic/thermodynamic environments*

Using 1000 J kg^{-1} and 20 m s^{-1} as axes and plotting events by month (Fig. 9a, similar to Tuovinen et al. 2015) revealed that most environments with SDOM characteristics occurred in the early season and that the same held true for CDOM environments and the late season. The mean CAPE and VWS for each convective environment could thus be placed into one of four dynamic/thermodynamic regimes: CDOM (>1000 J kg^{-1}, VWS < 20 m s^{-1}), SDOM (<1000 J kg^{-1}, VWS > 20 m s^{-1}), a "weak" regime (WEAK; CAPE < 1000 J kg^{-1}, VWS <20 m s^{-1}), and a "strong" regime (STRG; CAPE > 1000 J kg^{-1}, VWS > 20 m s^{-1}). These results are reflected in the categorical means shown in Fig. 9b, where the early season averaged data points were in the SDOM regime, while late-season averaged data points fell into the CDOM regime. CDOM and SDOM were dominated by events from their corresponding seasons. Note that a number of events from all months fell into the WEAK and/or STRG dynamic/thermodynamical regimes.

The breakdown of seasonal events by regime (Fig. 10) showed that SDOM led the early season count with 23 of 48 events (48%), and CDOM overwhelmingly dominated the late-season timeframe, making up 20 of 33 events (~60%). WEAK and STRG showed an even 11–11 split in the early season and a nearly even split in the late season. The two combined to nearly match the number of SDOM events in the cold season (22 total events; 46%) but only combined for half of the CDOM number in the warm season (~31%).

In summary, the early season was dominated by the SDOM environment, but more than half of possible hail-producing convective environments came from a different regime. The late season was less variable, with most possible hail-producing environments coming from the CDOM setup. Pairing this tendency with Fig. 4b highlights a relative minimum of high-CAPE, low-shear storm initiation outside of the near-SdC area in the late season. Additionally, WEAK and STRG appear to be as likely as the other to be a productive environment in either season. This result may be because for an SDOM environment to become CDOM (or vice versa), both CAPE and VWS would have to change. In contrast, for one of the seasonally dominant environments to become WEAK or STRG, only one parameter between CAPE and VWS would have to change.

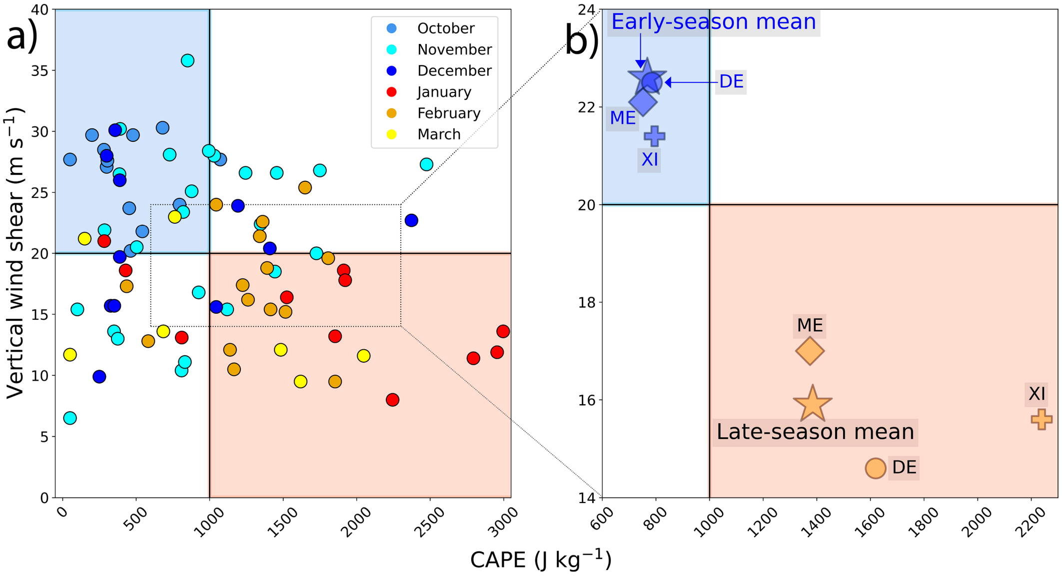

FIG. 9. Scatterplot of mean CAPE and vertical wind shear values for each convective event (a) by month and (b) for the mean seasonal values overall and per convective mode; the early season is in blue, and the late season is in orange. The gray dotted box in (a) represents the inset area in (b).

c. *Synoptic features of characteristic dynamic/thermodynamic environments*

To better understand the underlying dynamic and thermodynamic differences, we calculated composite synoptic characteristics of each regime (based on the ERA5 data) as anomalies against the means of the entire hail season (October–March). Notable features (see Figs. 11–13) include the warm and moist poleward flow known as the South American low-level jet (SALLJ; Saulo et al. 2000), a persistent, cold, and dry equatorward flow in the southwestern portion, low-level convergence near the SdC, and strong upper-level westerly winds blowing over the Andes.

1) SDOM FEATURES

As the high-shear, low-CAPE setup, the 850- and 250-hPa composite analyses highlight the features responsible for this regime. The 850-hPa analysis featured flow around a closed low pressure anomaly, shown by the clockwise rotation, to the southeast of the SdC with a trough extending northwestward (Figs. 11a and 12a). This rotation featured strong anomalously southerly winds between the SdC and the Andes and an enhancement of the SALLJ. At 250-hPa (Fig. 13a), the SDOM setup showed anomalous upper-level jets extending from the Andes eastward, with one branch flowing directly over the SdC and another to the southeast toward the Atlantic coast. These jets were fed by the cyclonic rotation around an upper-level low pressure anomaly to the southwest, as indicated by the anomalous lower geopotential heights. The combination of the strong low-level wind anomalies and the anomalous upper-level jets are likely key to creating the high-shear environments. Furthermore, the SdC straddle moderate positive and negative temperature (Fig. 11a) and moisture (Fig. 12a) anomalies. Given that the split between the 250-hPa jets indicated upper-level divergence over the region, this combination would aid in storm strengthening by adding a forcing mechanism in lieu of CAPE.

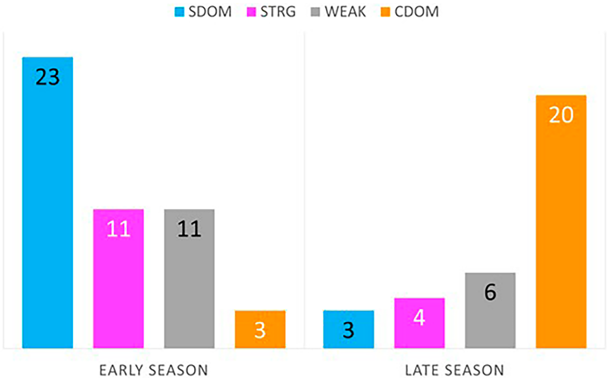

FIG. 10. Seasonal count of convective events per dynamic/thermodynamic regime.

These features indicate that the strong upper-level jet anomaly plus the enhanced low-level flows, combined with modest temperature and moisture anomalies, produced the low-CAPE, high-shear environment associated with SDOM. During RELÁMPAGO-CACTI, Varble et al. (2021) identified this prevailing pattern of strong upper-level westerly flow, which was shown to decrease in speed during the transition from the early to late season by Piersante et al. (2021). This tendency was reflected in the anomaly calculation as the December mean upper-level jet was much weaker than the October and November mean jets (not shown) as well as the continuous decrease in VWS from October through January (Fig. 8b).

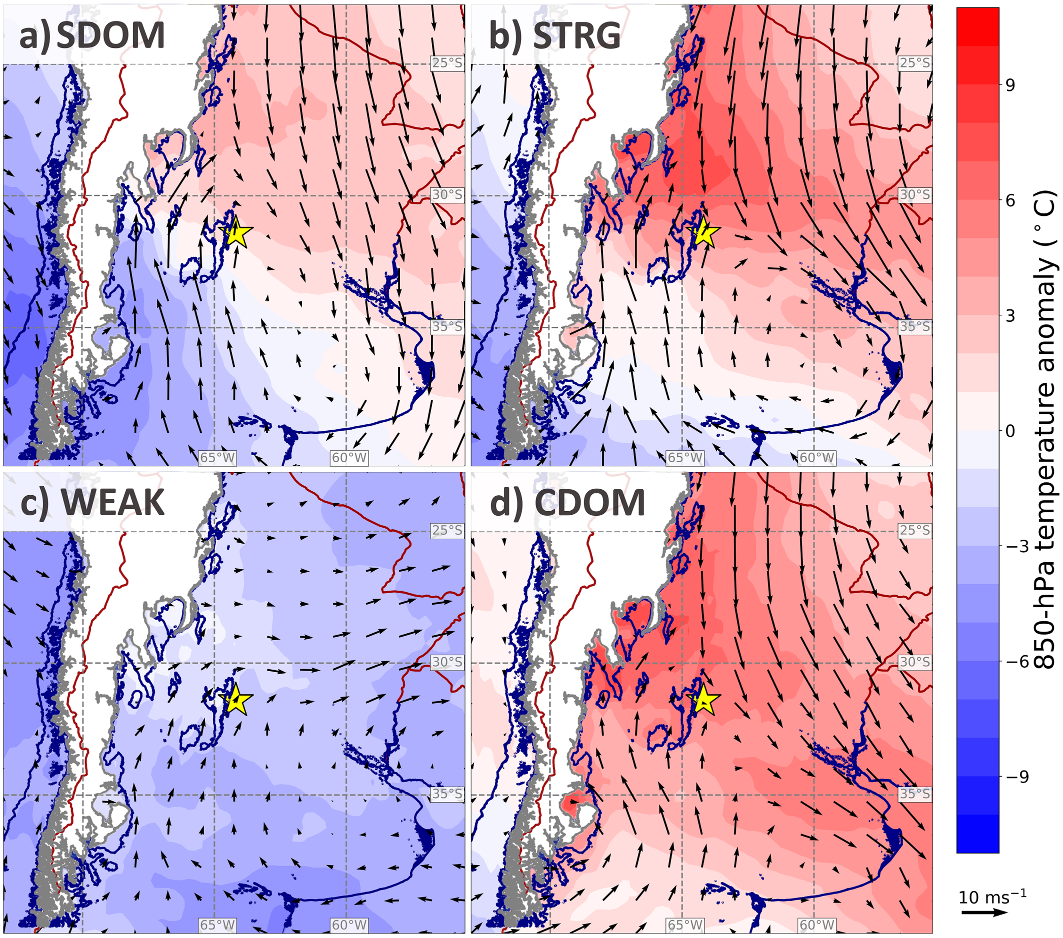

FIG. 11. 850-hPa temperature (shaded) and wind vector composite anomalies for convective events in (a) shear-dominant, (b) strong, (c) weak, or (d) CAPE-dominant regimes. The thick blue contour outlines a terrain height of 1000 m, highlighting the SdC and Andes mountain ranges. The yellow star indicates location of RMA1 radar. Red lines are noncoastal country borders.

The dynamics/thermodynamics at play in SDOM are revealed through deeper analysis of the anomalies. The dominant anomalous low and trough acted as the border between anomalously cool temperatures to the south and west and anomalously warm temperatures to the north and east (Fig. 11a). The dominant southerly flow crossed these isotherms, indicating cold air advection. To the northeast of the SdC, a slight anomalous enhancement of the SALLJ overlapped with a warm temperature anomaly, wrapping around the eastern portion of the cyclonic rotation near the coast. The general low-level moisture anomaly distribution showed moist conditions over most of the domain, with an anomalously dry slot to the south and west of the SdC (Fig. 12a). The low-level southerly flows originated in these areas of anomalously low moisture, while the northerly SALLJ drove the enhanced moisture southward to the area between the SdC and the Atlantic coast. This combination of anomalous low-level winds, temperature, and moisture was indicative of cold frontal systems moving into the area between the Andes and SdC, showing agreement with findings in Mezher et al. (2012). These systems would intersect with anomalously warm and moist air from the exit region of the SALLJ (Vera et al. 2006) and trigger deep convection (Salio et al. 2007; Saulo et al. 2007; Rasmussen and Houze 2011; Varble et al. 2021).

2) CDOM FEATURES

For the low-shear, high-CAPE CDOM regime, the closed low pressure anomaly associated with SDOM was not present, having been replaced by a trough extending from the Atlantic coast to the SdC (Figs. 11d and 12d). The lack of a closed circulation allowed the anomalous SALLJ to extend further to the south and southwest while maintaining elevated speeds. In contrast, the low-level wind anomalies immediately adjacent to the SdC were at a much lower magnitude, particularly when compared to SDOM. At 250 hPa (Fig. 13d), CDOM's strong anomalous upper-level jet maximum was in the southern part of the region with weak easterly anomalies directly over the SdC. Recall that Fig. 4b shows that most of the storm formation in the warm season occurs close to the SdC. These weak 850- and 250-hPa wind anomalies near the SdC indicate

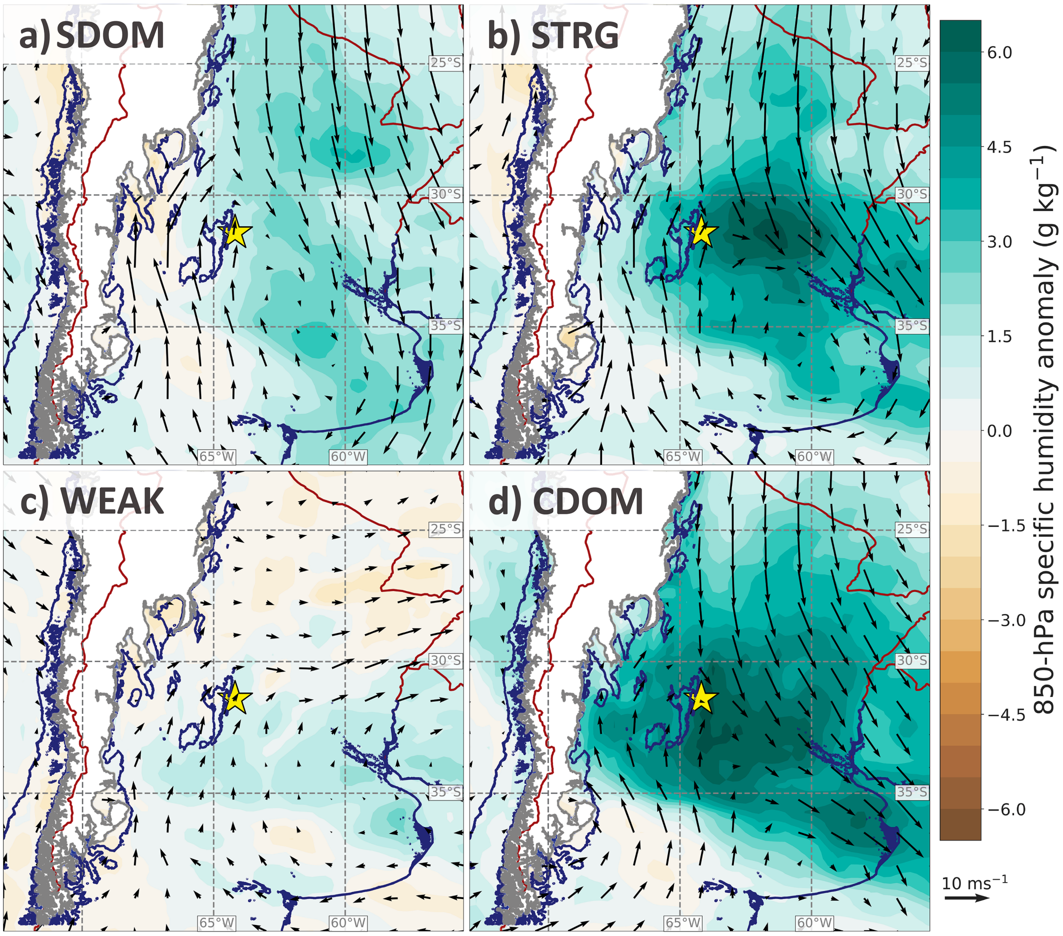

FIG. 12. As in Fig. 11, but with 850-hPa specific humidity composite anomalies (shaded).

a setup for weak shear. In further contrast to SDOM, the 850-hPa temperature (Fig. 11d) and moisture (Fig. 12d) anomalies were both positive, demonstrating favorable environments for high CAPE values.

The magnitude of the heat and moisture anomalies corresponded to the higher CAPE values, which when combined with the weakness of the lower- and upper-level wind anomalies directly over the SdC resulted in a high-CAPE, low-shear setup. Recall that PWAT values were higher during the late season, the timeframe that corresponds most to the CDOM setup. The enhanced PWAT values were reflected by the anomalously moist values in Fig. 12d. Additionally, this setup being so prevalent in the late season aligned with findings from Piersante et al. (2021), where their study of wide convective cores showed that synoptic forcing weakened in the late season, decreasing the number of smaller wide convective cores as the amount of large wide convective cores stayed the same. Consequently, the storms in the late season tended to form near the mountains, likely due to terrain-influenced mechanisms (Rasmussen and Houze 2016).

The anomalous enhancement of the SALLJ in this regime likely caused the domain to be dominated by anomalously high temperatures and high moisture values. The temperature anomalies displayed weaker gradients than for SDOM, with the strongest positive anomalies focused over the SdC and foothills of the Andes to the north (Fig. 11d). Strong flows through these high temperature areas resulted in large areas of weak warm air advection, i.e., the flow did not cross many isotherms. Additionally, there was still evidence of cold air advection as southerly winds crossed isotherms while approaching the SdC, as did the flow in the northeast portion of the domain. The highest values of the strong positive moisture anomaly (Fig. 12d) were located along and northeast of the low-level trough anomaly and at the intersection of the SALLJ and the anomalous southerly flow. Interestingly, the placement and magnitude of this moisture anomaly means that all flows into it would be considered anomalous dry advection, even for the anomalously moist flows coming from the north. An upper-level high pressure anomaly sat off the Atlantic coast, producing anticyclonic flow that enhanced the westerly jet maximum (Fig. 13d) but created a weaker and broader easterly flow to the north. The placement of the high pressure anomaly for CDOM at 250 hPa followed that of the anomalous setup for wide convective cores for September–November in Piersante et al. (2021).

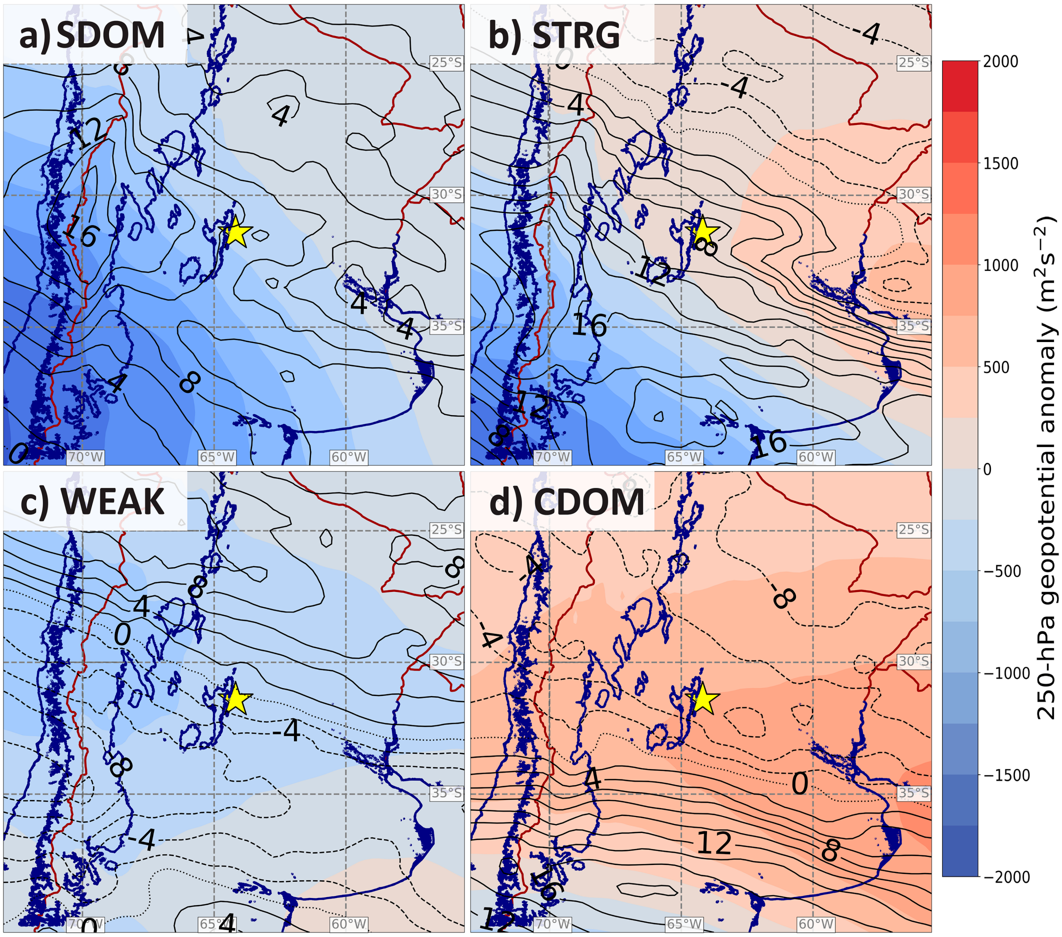

FIG. 13. As in Figs. 11 and 12, but for 250-hPa geopotential (shaded) and wind speed composite anomalies ($m\ s^{-1}$). Solid lines are positive (westerly) wind anomalies, and dashed lines are negative (easterly) wind anomalies.

3) STRG FEATURES

The STRG regime carried the dominant characteristics of both SDOM and CDOM. Mirroring SDOM, the 850-hPa winds showed a closed low pressure anomaly with a southerly flow between the Andes and SdC with a strong enhancement of the SALLJ (Figs. 11b and 12b). However, this SALLJ enhancement was more pronounced than either SDOM or CDOM, resulting in very strong offshore flow as the SALLJ intersected the low pressure anomaly. The 850-hPa winds in the immediate vicinity of the SdC were stronger than CDOM. The 250-hPa anomaly chart showed a dual-jet setup with a westerly/northwesterly configuration similar to SDOM but with higher wind speeds and more tightly packed isotachs (Fig. 13b). STRG displayed positive temperature anomalies along the SALLJ but featured negative anomalies to the south (Fig. 11b). Additionally, the location where the 850-hPa low pressure anomaly blocked and redirected the SALLJ flow was the location of the highest moisture anomalies (Fig. 12b). The low-level convergence caused by this intersection combined with the upper-level divergence due to the dual-jet setup increased lifting in this area.

The strong multidirectional low-level winds combined with the enhanced upper-level jets created the high shear in this environment, while the large positive temperature and moisture anomalies resulted in the high-CAPE. But while the high-CAPE and high-shear characteristics of STRG mirrored those of the dominant regimes, STRG retained some unique markers. The anomalous enhancement of the SALLJ drove the anomalous low-level heating but also brought (anomalous) cold-air advection to the region, indicated by winds moving from weaker warm anomalies to stronger in Fig. 11b. The anomalous warm-air advection flowed from the area with the highest temperature anomalies southeastward toward the coast. This resulted in a squeezing of the warm anomaly and the warm-air advection channel by cold-air advection from both sides. Anomalous dry flow was mostly collocated with the cold-air advection due to the strong gradients around the positive moisture anomaly (Fig. 12b). Strong westerly flow from the SdC area overlapped with the moisture anomaly and resulted in a very strong anomalous moist flow, which also likely enhanced PWAT values. At 250 hPa (Fig. 13b), STRG featured an anomalous upper-level high sitting just off the Atlantic coast (similar to CDOM) and a strong low pressure anomaly in the far southwest of the domain (similar to SDOM).

The flow between these two features is what created the amplified northeasterly jet over the SdC. The placement of the pressure anomalies for STRG at 250 hPa mirrored that of the anomalous setup for wide convective cores for December–February presented in Piersante et al. (2021).

4) WEAK FEATURES

In contrast to STRG, the WEAK regime featured environments conducive to neither large amounts of CAPE nor strong shear. As with SDOM and STRG, a low-level low pressure anomaly sat near the Atlantic coast (Figs. 11c and 12c). But instead of an anomalous enhancement of the SALLJ as seen with the other regimes, the area to the northeast of the SdC featured weak anomalous westerly low-level flow. At 250 hPa (Fig. 13c), wind speed anomalies were close to zero over the north side of the SdC and featured weak easterly anomalous flow over the south. With weak anomalous winds over the domain at both 850 and 250 hPa, there were no indicators of an environment conducive to high shear. Additionally, the entire domain displayed negative temperature anomalies (Fig. 11c) and weakly positive/negative moisture anomalies (Fig. 12c). The lack of heat and moisture do not portray an environment with robust CAPE values.

Because of the overall weakness of the anomalies, signatures of the WEAK regime were difficult to discern. Low-level southerly flow from south of the SdC and between the SdC and the Andes curved cyclonically into the weak westerly flow, which led to a decrease in low-level convergence near the SdC. The arrangement of the temperature anomaly isotherms showed very weak cold air advection from the south and weak warm air advection originating from the Andes north of the SdC (Fig. 11c). The weak positive moisture anomalies were located to the south of the SdC extending to the coast (Fig. 12c). Weak anomalous dry advection circled around the coastal low from the south, and weak moist advection flowed into the anomalous low-level westerlies. WEAK displayed an upper-level low pressure anomaly located over the Andes, centered much further north than SDOM or STRG. This positioning resulted in upper-level westerly anomalies to the north and easterly anomalies to the south.

5. Conclusions

A survey of ground-based operational radar characteristics in the Córdoba region identified the convective and initiation modes of hail-producing convective cells for the 2018–19 hail season of central Argentina. Hail reports were obtained from three sources: direct observation from the RELÁMPAGO field campaign, Twitter posts that reported hail and could be positively cross-referenced with data from the C-band RMA1 radar, and radar identification using likely hail-producing signatures through RMA1's dual-polarized parameters. ERA5 analysis of the grouped convective events identified four characteristic dynamic/thermodynamic environments divided along a threshold of 20 m s^{-1} vertical wind shear and 1000 J kg^{-1} CAPE. Composite analysis of the cases characterized by these environments indicates that differences in the positioning of the SALLJ, upper-level jets, and temperature and moisture anomalies impact the initiation and convective mode of hail-producing storms throughout the season.

Results show that over the 6 months of data gathered, the most common type of hail-producing convective mode was discrete convection. This result held true whether counting individual cells or counting convective events that contained one or more discrete cells. However, there were differences as seasons changed. Unlike the discrete dominant October–December timeframe, January–March convective events were virtually even between discrete and multicells. Bruick et al. (2019)—a satellite-based study—states that ~84% of the hailstorms documented in their study fell into their organized multicellular convection category. While this radar-based study is limited in scope (one severe-weather season; ~150 data points), it does raise the possibility that this contrast may indicate a classification difference owing to satellite- versus radar-based techniques. A larger database of radar-captured hail events is needed to further examine this difference.

Figure 14 conceptualizes the differences in composite environmental setups seen throughout the hail season. Grouping environments based on CAPE and surface-to-500-hPa vertical wind shear led to the discovery that early season storm environments favored a low-CAPE, high-shear setup (SDOM), while late season overwhelmingly saw high-CAPE, low-shear environments (CDOM). Further analysis revealed that the SDOM setup (Fig. 14a) featured a strong jet over the Sierras de Córdoba and migrating shortwaves, while the CDOM setup (Fig. 14d) consisted of weak lower- and upper-level winds over the SdC and strong heat and moisture anomalies, leading to hail production focused in the SdC area. The high-CAPE, high-shear STRG setup (Fig. 14b) blends strong temperature and dewpoint anomalies with strong upper-level winds, while the low-CAPE, low-shear WEAK category (Fig. 14c) does not feature migrating shortwaves or a strong jet. STRG and WEAK environments were split nearly evenly within each season. All setups feature some kind of westerly upper-air jet, similar to what was outlined in Mezher et al. (2012). It is important to note that the primacy of the Andes and the Sierras de Córdoba in numerical simulations has confirmed that both mountain ranges aid in strengthening storm parameters (VWS, cold pools; Rasmussen and Houze 2016; Mulholland et al. 2019), causing upsloping (Varble et al. 2021), and being a main reason why the SALLJ exists at all (Insel et al. 2010).

These results should be seen within the bounds of their limitations. While radar is ideal for identifying convective modes, using it to identify which cells are producing hail will leave gaps. Using the polarimetric variables is reliable, but melting hail can increase beam attenuation, resulting in false values (Ryzhkov et al. 2013). Satellite data have trouble resolving smaller cells (beamwidth, limited horizontal resolution, and beam attenuation; Heymsfield et al. 2000), but their potential geographic coverage enables the gathering of many more data points when compared to that of a solitary, stationary ground-based system. This coverage limitation results in studies limited to one solitary radar having far less raw data to work for comparative analyses. The focus on operational radar data without a wide network of frequent surface and upper-air observations makes it difficult to examine the methods of storm initiation (e.g., outflow boundaries, terrain influenced). While RMA1 is subject to beam blocking by the SdC, the ability

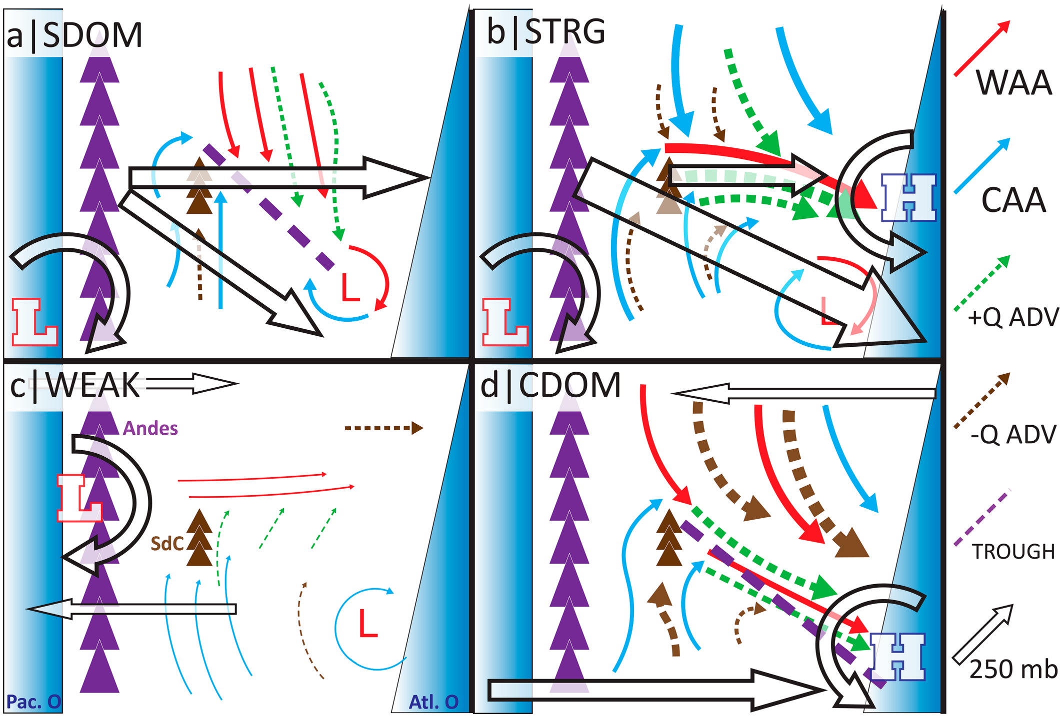

FIG. 14. Conceptual models of each dynamic/thermodynamic regime. Arrow thickness indicates the relative strength of flow/advection. Figure is not to scale.

to identify and track storms on the west side of the range ameliorates some of the concern that observation numbers have been thrown off. The use of three-body scatter spikes did not seem to introduce a bias toward hail size (Zrnić et al. 2010), but since this study does not take hail size into account, it is possible that storms with smaller hail were not detected. Also, because of the possibility of noisy returns on radar, three-body scatter spikes stand out more with discrete cells as opposed to multicells, which can introduce bias. The inability of ERA5 data to resolve smaller features can lead to artifacts such as the 0 CAPE measurements for some vertical profiles.

Another limitation is data availability. Owing to data acquisition constraints stemming from the COVID-19 pandemic, this study only examines one severe-weather season. With only 162 cells, then packaged into 81 convective events, calculations of means and anomalies have limited data points to use (recall that March only had seven recorded convective events). While broad climatological conclusions can thusly not be drawn from these cases, this study was able to identify useful relationships between convective modes and their respective environments. Expansion on this research would include repeating this study over numerous convective seasons as the RMA1 dataset grows. If the identified relationships between convective modes and the identified dynamic/thermodynamic regimes hold up to future research, that would give forecasters in this region tools with which to be prepared for hail-producing events. Future research will also expand on cell initiation modes as possible nowcasting indicators.

Acknowledgments. The authors thank the U.S. Air Force for sponsoring and supporting the dissertation research of the lead author. Additionally, the authors appreciate the insights of Sonia Lasher-Trapp, Stephen Nesbitt, and Robert Trapp, as well as the reviewers, who significantly improved the paper. They gratefully acknowledge Paola Salio, Martin Runga, and others from Universidad de Buenos Aires and Servicio Meteorológico Nacional for local insight; Proyecto RELÁMPAGO for data collection; Jake Mulholland for helpful discussion; and Randy Chase for computational assistance. This research was supported by the National Science Foundation under Grant AGS-1943553. The views expressed in this paper are those of the authors and do not necessarily reflect the official policy or position of the U.S. Air Force, the Department of Defense, or the U.S. government.

Data availability statement. Data analyzed in this study were a combination of reanalysis data, which are openly available through the European Centre for Medium-Range Weather Forecasts (https://www.ecmwf.int/en/forecasts/dataset/ecmwf-reanalysis-v5), radar data from RMA1 (data from RELÁMPAGO are available at https://doi.org/10.26023/TTK1-C4VG-VG0K; other data available by request from SMN), and Twitter data, which are publicly available (though subject to account changes and post deletion). Brandwatch services can be found on their website (https://www.brandwatch.com/), but University of Illinois Brandwatch access is limited to university personnel. General information about and data from RELÁMPAGO are available in the field catalog, available at http://catalog.eol.ucar.edu/relampago/tools/missions.

APPENDIX A

Manual Storm Cell Tracking

Figure A1 is an outline of the method used to track cells that were added to the storm database for the purpose of identifying initiation time and location. This method begins after hail detection and convective mode have been identified and the cell is added to database. Note that the "initiation mode" is a parameter to be used for future research.

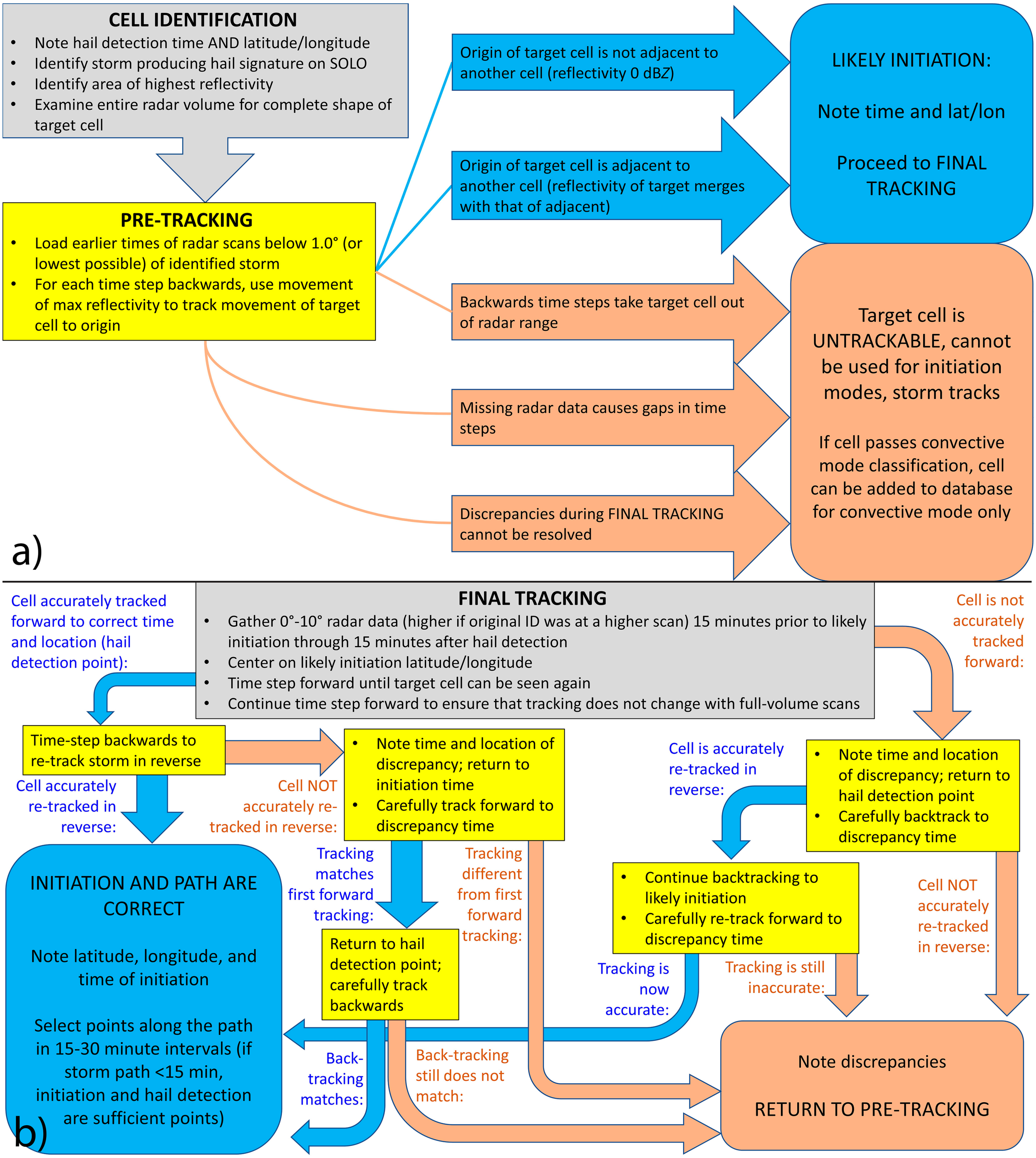

FIG. A1. Flow diagram of methodology used to track cells identified as hail containers. (a) Cell identification and pretracking. (b) Final tracking.

APPENDIX B

Convective Event Grouping

Figure B1 is an overview of how individual cells were grouped into convective events.

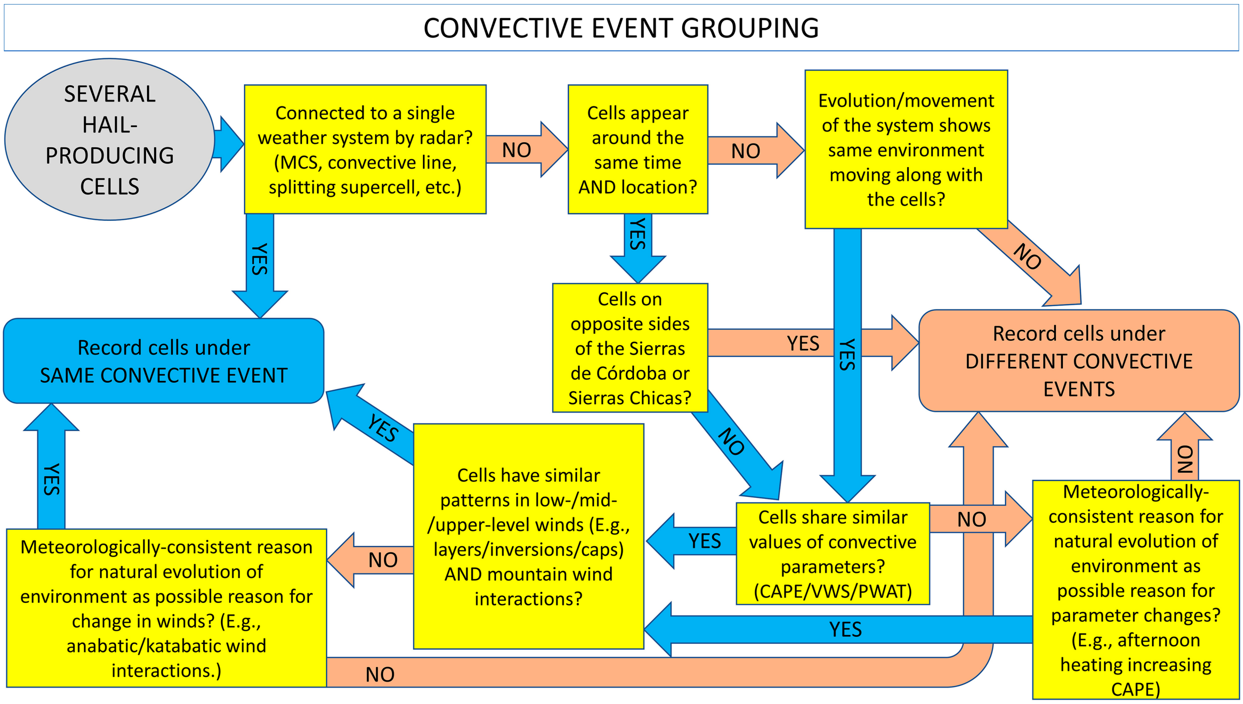

FIG. B1. Flow diagram of methodology used to group individual cells into convective events (when necessary).

REFERENCES

Allen, J. T., D. J. Karoly, and G. A. Mills, 2011: A severe thunderstorm climatology for Australia and associated thunderstorm environments. *Aust. Meteor. Oceanogr. J.*, **61**, 143–158, https://doi.org/10.22499/2.6103.001.

Anderson, M. E., L. D. Carey, W. A. Petersen, and K. R. Knupp, 2011: C-band dual-polarimetric radar signatures of hail. *Electron. J. Oper. Meteor.*, **12**, 1–30.

Bluestein, H. B., and M. H. Jain, 1985: Formation of mesoscale lines of precipitation: Severe squall lines in Oklahoma during the spring. *J. Atmos. Sci.*, **42**, 1711–1732, https://doi.org/10.1175/1520-0469(1985)042<1711:FOMLOP>2.0.CO;2.

Bruick, Z. S., K. L. Rasmussen, and D. J. Cecil, 2019: Subtropical South American hailstorm characteristics and environments. *Mon. Wea. Rev.*, **147**, 4289–4304, https://doi.org/10.1175/MWR-D-19-0011.1.

Carey, L. D., S. A. Rutledge, D. A. Ahijevych, and T. D. Keenan, 2000: Correcting propagation effects in C-band polarimetric radar observations of tropical convection using differential propagation phase. *J. Appl. Meteor.*, **39**, 1405–1433, https://doi.org/10.1175/1520-0450(2000)039<1405:CPEICB>2.0.CO;2.

Cecil, D. J., 2009: Passive microwave brightness temperatures as proxies for hailstorms. *J. Appl. Meteor. Climatol.*, **48**, 1281–1286, https://doi.org/10.1175/2009JAMC2125.1.

——, and C. B. Blankenship, 2012: Toward a global climatology of severe hailstorms as estimated by satellite passive microwave imagers. *J. Climate*, **25**, 687–703, https://doi.org/10.1175/JCLI-D-11-00130.1.

Evans, J. S., and C. A. Doswell III, 2001: Examination of derecho environments using proximity soundings. *Wea. Forecasting*, **16**, 329–342, https://doi.org/10.1175/1520-0434(2001)016<0329:EODEUP>2.0.CO;2.

Fabry, F., 2015: *Radar Meteorology: Principles and Practice*. Cambridge University Press, 256 pp.

Fraustino, J. D., B. Liu, and J. Yan, 2012: Social media use during disasters: A review of the knowledge base and gaps. National Consortium for the Study of Terrorism and Responses to Terrorism, 39 pp., https://www.start.umd.edu/publication/social-media-use-during-disasters-review-knowledge-base-and-gaps.

Gallus, W. A., Jr., N. A. Snook, and E. V. Johnson, 2008: Spring and summer severe weather reports over the Midwest as a function of convective mode: A preliminary study. *Wea. Forecasting*, **23**, 101–113, https://doi.org/10.1175/2007WAF2006120.1.

Gematronik, 2007: *Dual-Polarization Weather Radar Handbook*. 2nd ed. Selex-SI Gematronik, 163 pp.

Helmus, J. J., and S. M. Collis, 2016: The Python ARM Radar Toolkit (Py-ART), a library for working with weather radar data in the Python programming language. *J. Open Res. Software*, **4**, e25, https://doi.org/10.5334/jors.119.

Hersbach, H., and Coauthors, 2020: The ERA5 global reanalysis. *Quart. J. Roy. Meteor. Soc.*, **146**, 1999–2049, https://doi.org/10.1002/qj.3803.

Heymsfield, G. M., B. Geerts, and L. Tian, 2000: TRMM precipitation radar reflectivity profiles as compared with high-resolution airborne and ground-based radar measurements. *J. Appl. Meteor.*, **39**, 2080–2102, https://doi.org/10.1175/1520-0450(2001)040<2080:TPRRPA>2.0.CO;2.

Insel, N., C. J. Poulsen, and T. A. Ehlers, 2010: Influence of the Andes Mountains on South American moisture transport, convection, and precipitation. *Climate Dyn.*, **35**, 1477–1492, https://doi.org/10.1007/s00382-009-0637-1.

Johns, R. H., 1993: Meteorological conditions associated with bow echo development in convective storms. *Wea. Forecasting*, **8**, 294–299, https://doi.org/10.1175/1520-0434(1993)008<0294:MCAWBE>2.0.CO;2.

Kaltenboeck, R., and A. Ryzhkov, 2012: Comparison of polarimetric radar signatures in hailstorms simultaneously observed by C-band and S-band radars. *ERAD 2012: Seventh European Conf. on Radar in Meteorology and Hydrology*, Toulouse, France, Météo-France, http://www.meteo.fr/cic/meetings/2012/ERAD/extended_abs/MIC_165_ext_abs.pdf.

Kumjian, M. R., and Coauthors, 2020: Gargantuan hail in Argentina. *Bull. Amer. Meteor. Soc.*, **101**, E1241–E1258, https://doi.org/10.1175/BAMS-D-19-0012.1.

Lemon, L. R., 1998: The radar “three-body scatter spike”: An operational large-hail signature. *Wea. Forecasting*, **13**, 327–340, https://doi.org/10.1175/1520-0434(1998)013<0327:TRTBSS>2.0.CO;2.

Li, M., D.-L. Zhang, J. Sun, and Q. Zhang, 2018: A statistical analysis of hail events and their environmental conditions in China during 2008–15. *J. Appl. Meteor. Climatol.*, **57**, 2817–2833, https://doi.org/10.1175/JAMC-D-18-0109.1.

Liu, B. F., J. D. Fraustino, and Y. Jin, 2016: Social media use during disasters: How information form and source influence intended behavioral responses. *Commun. Res.*, **43**, 626–646, https://doi.org/10.1177/0093650214565917.

Martins, J. A., and Coauthors, 2017: Climatology of destructive hailstorms in Brazil. *Atmos. Res.*, **184**, 126–138, https://doi.org/10.1016/j.atmosres.2016.10.012.

May, R. M., and Coauthors, 2020: MetPy: A Python package for meteorological data, version 0.12.2. Unidata, accessed 29 September 2021, https://doi.org/10.5065/D6WW7G29.

Mezher, R. N., M. Doyle, and V. Barros, 2012: Climatology of hail in Argentina. *Atmos. Res.*, **114–115**, 70–82, https://doi.org/10.1016/j.atmosres.2012.05.020.

Mulholland, J. P., S. W. Nesbitt, R. J. Trapp, K. L. Rasmussen, and P. V. Salio, 2018: Convective storm life cycle and environments near the Sierras de Córdoba, Argentina. *Mon. Wea. Rev.*, **146**, 2541–2557, https://doi.org/10.1175/MWR-D-18-0081.1.

——, ——, and ——, 2019: A case study of terrain influences on upscale convective growth of a supercell. *Mon. Wea. Rev.*, **147**, 4305–4324, https://doi.org/10.1175/MWR-D-19-0099.1.

Nesbitt, S. W., and Coauthors, 2021: A storm safari in subtropical South America: Proyecto RELAMPAGO. *Bull. Amer. Meteor. Soc.*, **102**, E1621–E1644, https://doi.org/10.1175/BAMS-D-20-0029.1.

Pavlov, A. K., and Coauthors, 2018: Does your lab use social media?: Sharing three years of experience in science communication. *Bull. Amer. Meteor. Soc.*, **99**, 1135–1146, https://doi.org/10.1175/BAMS-D-17-0195.1.

Piersante, J. O., K. L. Rasmussen, R. S. Schumacher, A. K. Rowe, and L. A. McMurdie, 2021: A synoptic evolution comparison of the smallest and largest MCSs in subtropical South America between spring and summer. *Mon. Wea. Rev.*, **149**, 1943–1966, https://doi.org/10.1175/MWR-D-20-0208.1.

Rasmussen, K. L., and R. A. Houze Jr., 2011: Orogenic convection in subtropical South America as seen by the TRMM satellite. *Mon. Wea. Rev.*, **139**, 2399–2420, https://doi.org/10.1175/MWR-D-10-05006.1.

——, and ——, 2016: Convective initiation near the Andes in subtropical South America. *Mon. Wea. Rev.*, **144**, 2351–2374, https://doi.org/10.1175/MWR-D-15-0058.1.

Rauber, R. M., and S. W. Nesbitt, 2018: *Radar Meteorology, an Introduction*. Wiley Blackwell, 461 pp.

Ryzhkov, A. V., M. R. Kumjian, S. M. Ganson, and P. Zhang, 2013: Polarimetric radar characteristics of melting hail. Part II: Practical implications. *J. Appl. Meteor. Climatol.*, **52**, 2871–2886, https://doi.org/10.1175/JAMC-D-13-074.1.

Salio, P., M. Nicolini, and E. J. Zipser, 2007: Mesoscale convective systems over southeastern South America and their relationship with the South American low-level jet. *Mon. Wea. Rev.*, **135**, 1290–1309, https://doi.org/10.1175/MWR3305.1.

Saulo, A. C., M. Nicolini, and S. C. Chou, 2000: Model characterization of the South American low-level flow during the 1997–1998 spring–summer season. *Climate Dyn.*, **16**, 867–881, https://doi.org/10.1007/s003820000085.

——, J. Ruiz, and Y. G. Skabar, 2007: Synergism between the low-level jet and organized convection at its exit region. *Mon. Wea. Rev.*, **135**, 1310–1326, https://doi.org/10.1175/MWR3317.1.

Schumacher, R. S., and Coauthors, 2021: Convective-storm environments in subtropical South America from high-frequency soundings during RELAMPAGO-CACTI. *Mon. Wea. Rev.*, **149**, 1439–1458, https://doi.org/10.1175/MWR-D-20-0293.1.

Smith, B. T., R. L. Thompson, J. S. Grams, C. Broyles, and H. E. Brooks, 2012: Convective modes for significant severe thunderstorms in the contiguous United States. Part I: Storm classification and climatology. *Wea. Forecasting*, **27**, 1114–1135, https://doi.org/10.1175/WAF-D-11-00115.1.

Trapp, R. J., S. A. Tessendorf, E. S. Godfrey, and H. E. Brooks, 2005: Tornadoes from squall lines and bow echoes. Part I: Climatological distribution. *Wea. Forecasting*, **20**, 23–34, https://doi.org/10.1175/WAF-835.1.

Tuovinen, J.-P., J. Rauhala, and D. M. Schultz, 2015: Significant-hail-producing storms in Finland: Convective-storm environment and mode. *Wea. Forecasting*, **30**, 1064–1076, https://doi.org/10.1175/WAF-D-14-00159.1.

Varble, A. C., and Coauthors, 2021: Utilizing a storm-generating hotspot to study convective cloud transitions: The CACTI experiment. *Bull. Amer. Meteor. Soc.*, **102**, E1597–E1620, https://doi.org/10.1175/BAMS-D-20-0030.1.

Velasco, I., and J. M. Fritsch, 1987: Mesoscale convective complexes in the Americas. *J. Geophys. Res.*, **92**, 9591–9613, https://doi.org/10.1029/JD092iD08p09591.

Vera, C., and Coauthors, 2006: The South American Low-Level Jet Experiment. *Bull. Amer. Meteor. Soc.*, **87**, 63–78, https://doi.org/10.1175/BAMS-87-1-63.

Wilson, J. W., and D. Reum, 1986: “The hail spike”: Reflectivity and velocity signature. Preprints, *23rd Conf. on Radar Meteorology*, Snowmass, CO, Amer. Meteor. Soc., 62–65.

——, and ——, 1988: The flare echo: Reflectivity and velocity signature. *J. Atmos. Oceanic Technol.*, **5**, 197–205, https://doi.org/10.1175/1520-0426(1988)005<0197:TFERAV>2.0.CO;2.

Zipser, E. J., D. J. Cecil, C. Liu, S. W. Nesbitt, and D. P. Yorty, 2006: Where are the most intense thunderstorms on Earth? *Bull. Amer. Meteor. Soc.*, **87**, 1057–1072, https://doi.org/10.1175/BAMS-87-8-1057.

Zrnić, D. S., 1987: Three-body scattering produces precipitation signature of special diagnostic value. *Radio Sci.*, **22**, 76–86, https://doi.org/10.1029/RS022i001p00076.

——, G. Zhang, V. Melnikov, and J. Andric, 2010: Three-body scattering and hail size. *J. Appl. Meteor. Climatol.*, **49**, 687–700, https://doi.org/10.1175/2009JAMC2300.1.